Journal of Materials Chemistry B

ROYAL SOCIETY OF CHEMISTRY

PAPER

View Article Online
View Journal | View Issue

Cite this: J. Mater. Chem. B, 2024, 12, 7384

Cationic-motif-modified exosomes for mRNA delivery to retinal photoreceptors†

Héctor A. Millán Cotto,[a] Tanvi Vinod Pathrikar,[a] Bill Hakim,[a] Helna M. Baby,[a] Hengli Zhang,[a] Peng Zhao,[b] Ronak Ansaripour,[a] Rouzbeh Amini,[ac] Rebecca L. Carrier[ab] and Ambika G. Bajpayee *[abc]

Topical treatment of vitreoretinal diseases remains a challenge due to slow corneal uptake and systemic clearance. Exosomes are emerging nanocarriers for drug delivery due to biocompatibility and cellular targeting properties. To apply them for retinal targeting *via* the topical route, exosomes must traverse various ocular barriers including the cornea, lens, vitreous humor (VH), and the retina itself. Here we engineered high-purity milk-derived exosomes by anchoring arginine-rich cationic motifs *via* PEG_{2000} lipid insertion on their surface. Modification enabled exosomes to use weak-reversible electrostatic interactions with anionic glycosaminoglycan (GAG) and water content of the tissue to enhance their transport rate and retention. Addition of cationic motifs neutralized the anionic surface charge of exosomes (−24 to −2 mV) without impacting size or morphology. Cationic-motif-modified exosomes exhibited two-fold faster steady state diffusivity through bovine corneas compared to unmodified exosomes. Fluorescence recovery after photobleaching confirmed that cationic-motif-modified exosomes can diffuse through VH without steric hindrance. In healthy VH, cationic-motif-modified exosomes demonstrated stronger binding resulting in three-fold lower average diffusivity that enhanced by six-fold in 50% GAG-depleted VH recapitulating advanced liquefaction. Cationic-motif-modified exosomes penetrated through the full-thickness of porcine retinal explants resulting in ten-fold higher uptake in photoreceptors and three-fold greater transfection with encapsulated eGFP mRNA compared to unmodified exosomes. Cationic-motif-modified exosomes are safe to use as they did not adversely affect the mechanical swelling properties of the cornea or lens nor impact retinal cell viability. Cationic-motif-modified exosomes, therefore, offer themselves as a cell-free nanocarrier platform for gene delivery to retinal photoreceptors potentially *via* the topical route.

Received 18th April 2024,
Accepted 24th June 2024

DOI: 10.1039/d4tb00849a

rsc.li/materials-b

1 Introduction

Vitreoretinal diseases remain a challenge due to a lack of reliable retinal-targeting treatment options.[1,2] Invasive methods, like injections and ocular implants, can only be used sparingly because they incur increasing risks of retinal detachment, cataracts, and intraocular pressure destabilization when used repeatedly.[2–6] Topical treatment would prevent these risks but is currently not feasible due to slow corneal uptake, which results in ~90% loss of the therapeutic.[7–12] Both delivery modes suffer from fast clearance and low retinal targeting. Over the last decade, there has been a growing interest in developing polymeric and liposomal based synthetic nano-carriers to surmount these challenges, but their translatability has been limited by issues like high cytotoxicity, immunogenicity, lipophilicity-induced aggregation leading to vision occlusion, and a lack of retinal targeting.[2,7]

Exosomes are cell-derived extracellular vesicles that play an important role in intercellular communication *via* genetic material and growth factors acquired from the host cells.[13] They have been applied in targeted drug delivery to a variety of tissues owing to their non-immunogenicity, stability, and cellular targeting properties.[13–20] In recent work, cell derived exosomes have been used as nanocarriers to deliver small molecule drugs and gene-based therapeutics to the retina.[16,21–23] However, to be used for retinal cell-targeting *via* the topical route, exosomes must be able to navigate through various ocular tissue barriers including the cornea, lens, vitreous humor (VH), and the retina itself (Fig. 1). Their intrinsic physicochemical properties facilitate overcoming

[a] Department of Bioengineering, Northeastern University, Boston, MA, 02115, USA. E-mail: millancotto.h@northeastern.edu, pathrikar.t@northeastern.edu, hakim.bi@northeastern.edu, baby.h@northeastern.edu, zhang.hengli@northeastern.edu, ansaripour.r@northeastern.edu, r.amini@northeastern.edu, rebecca@coe.northeastern.edu, a.bajpayee@northeastern.edu; Tel: +1 617-373-7018
[b] Department of Chemical Engineering, Northeastern University, Boston, MA 02115, USA. E-mail: pe.zhao@northeastern.edu
[c] Department of Mechanical and Industrial Engineering, Northeastern University, Boston, MA 02115, USA

† Electronic supplementary information (ESI) available. See DOI: https://doi.org/10.1039/d4tb00849a

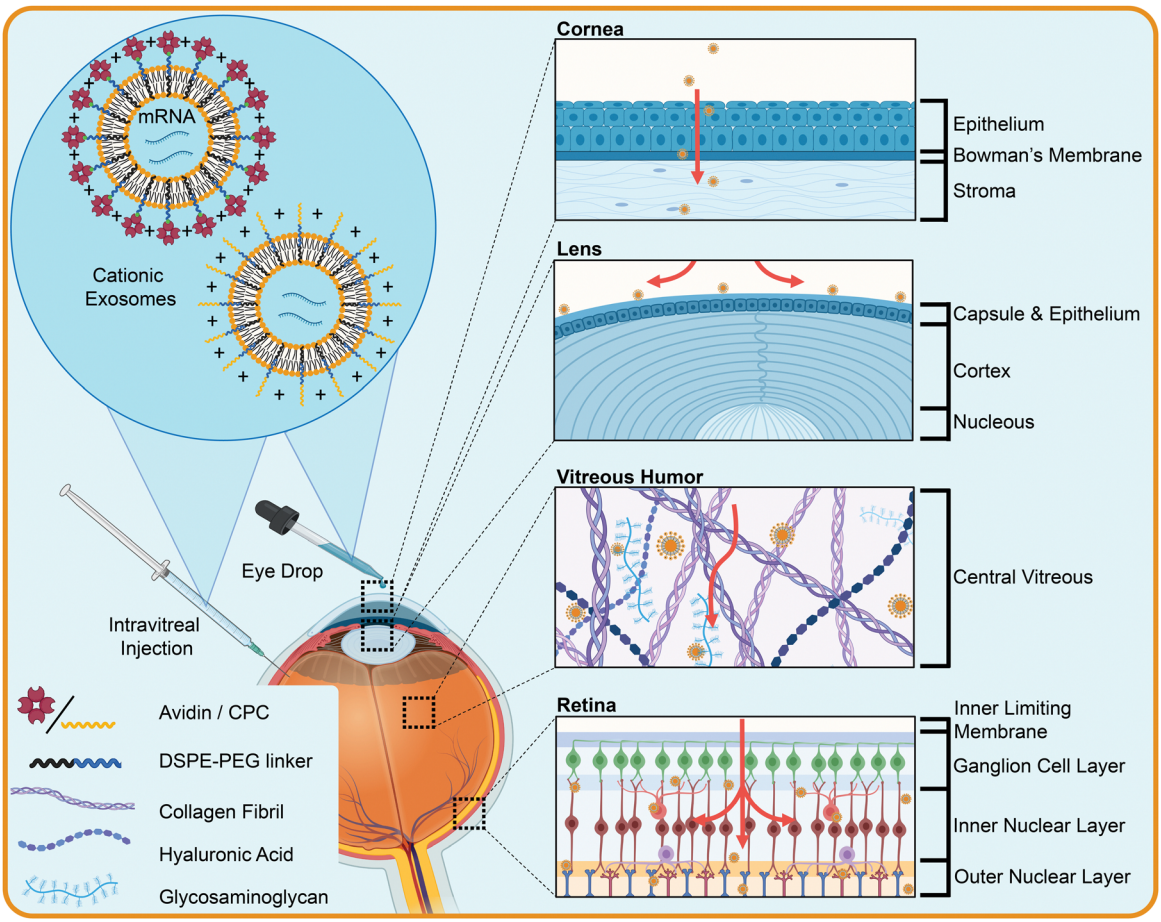

Fig. 1 Cationic-motif-modified exosomes (Exo) have the potential to reach the anterior-eye following either topical application or through intravitreal injections. Their charge-neutralized PEGylated surface increases both hydrophilicity and weak-reversible binding interactions with anionic eye tissue components. Consequently, cationic-motif-modified Exo can penetrate faster through the cornea due to the added Coulombic attraction between the cationic motifs and the anionic tissue. Moreover, their lipophilicity allows them to penetrate the corneal epithelium intracellularly and their hydrophilicity facilitates diffusion through the stroma. Exo that reach the lens are too large for penetration and therefore do not affect the electro-mechano-chemical balance of the tissue. In the vitreous humor, charge interactions slow down their diffusion creating a drug depot. Finally, as the Exo reach the retina, the cationic motifs improve their cellular uptake and reach photoreceptors *via* endocytosis. Created with BioRender.com.

only some of these challenges. For instance, their lipid bilayer allows them to avoid the tight junction of the corneal epithelial layer by penetrating intracellularly.[24,25] The size of exosomes ranges between 30 to 250 nm, which allows them to circumnavigate the lens capsule that has a pore size smaller than 20 nm and is known to trap small drugs.[26–29] Moreover, exosomes are small enough to diffuse through the 500 nm pore size of VH without steric hindrance.[30–32]

To enable their anterior-to-posterior transport needed for topical delivery, exosomes can be modified to take advantage of the anionic glycosaminoglycan (GAG) and water content of the tissue. The GAG content in the cornea gives it a negative fixed charge density (FCD) of −50 mM;[33,34] thus, introducing cationic motifs onto the anionic lipid bilayer of exosomes allows them to cling onto the corneal surface thereby minimizing getting flushed out into the systemic flow by the tear film.[24,33] Moreover, the cornea is 78% water, most of which is in the stroma, implying that imparting greater hydrophilicity to exosome surface could enhance their transport through the stroma.[25] Similarly, hydrophilic carriers have shown rapid diffusion through the VH, which is 98% water.[30,31] The solid matrix of the VH is composed of about 70% collagen and 30% GAGs; the GAGs are comprised of 96% hyaluronic acid and about 4% of uniformly distributed chondroitin and heparin sulfate GAGs, giving the VH a low negative FCD of −0.5 mM.[32] In older patients, vitreous liquefaction is associated with up to a 50% loss of collagen and GAG content, and aggregation of collagen fibrils combined with increased water content.[32,35] Regardless of age, interactions with the GAG and water content within these tissues will dictate exosome transport across the eye. Therefore, we hypothesize that intra-ocular transport properties of exosomes can be enhanced by modifying their anionic surface to introduce cationic charges and increase hydrophilicity. These modifications would allow modified exosomes to effectively diffuse from the front to the back of the eye by taking advantage of weak-reversible charge-based binding interactions to transport across the cornea, both healthy and degenerated vitreous, and penetrate deep into the retina. Our group has established a low-cost method for harvesting a high yield and high purity bovine-milk derived

exosomes by combining casein chelation with differential ultracentrifugation followed by size exclusion chromatography.[17] We have also developed methods for surface modification of exosomes *via* lipid insertion and click chemistry.[17,36] We have employed these techniques to conjugate hydrophilic and zwitterionic motifs onto milk-derived exosomes to improve their intestinal mucin transport for applications in oral gene delivery.[17,36] We recently designed charge-reversed exosomes for delivering drugs to chondrocytes residing in deep layers of avascular, anionic and aggrecan rich cartilage tissue.[37]

The goal of this study was to engineer retinal targeting milk-derived exosomes for mRNA delivery to retinal cells *via* the topical route. To that end, exosomes were surface modified *via* anchoring of (i) cationic motifs to neutralize their net negative charge and (ii) PEG motifs to enhance their surface hydrophilicity. A 66 kDa basic glycoprotein, Avidin (Av) and a short 20 AA long arginine and polar asparagine rich cationic peptide carrier (CPC, RRRR(NNRRR)$_3$R) of net +14 charge conjugated to PEG_{2000} were used as surface anchoring motifs to synthesize two cationic-motif-modified exosome formulations, Exo-Av and Exo-CPC. These modifications neutralized their anionic surface charge without significantly impacting morphology or size. Our non-equilibrium intra-tissue transport characterization revealed that cationic-motif-modified exosomes diffused faster than unmodified exosomes across the cornea and in GAG-depleted VH but were slower in the healthy VH owing to charge-based binding with negatively charged GAG binding sites. Exosomes were found to be safe and did not impact the electro-mechano-chemical properties of the tissue. Using a porcine retina explant culture model, our results show that Exo-CPC transported across the entire retina, from the inner limiting membrane (ILM) through the outer neuronal layer (ONL, Fig. 1), and effectively transfected the photoreceptors residing in the retinal ONL with the encapsulated eGFP mRNA. Native unmodified exosomes were ineffective in targeting the deep retinal layers. These findings, for the first time, demonstrate the potential of milk-derived cationic-motif-modified exosomes for mRNA delivery to photoreceptors in the retina *via* the topical route.

2 Materials and Methods

2.1 Materials

Cationic peptide carriers of +14 net charge (CPC), sequence: RRRR(NNRRR)$_3$R, were synthesized by MIT Biopolymers and Proteomics (Cambridge, MA). 1,2-Distearoyl-*sn-glycero*-3-phosphoethanolamine-*N*-[maleimide(polyethyleneglycol)-2000] (ammonium salt) (DSPE-PEG-malemide) was purchased from Avanti Polar Lipids (Alabaster, AL). Phosphate-buffered saline (PBS), trypsin-EDTA, dimethylformamide (DMF), fluorescein isothiocyanate (FITC), 4′,6-diamidino-2-phenylindole, dihydrochloride (DAPI), 3 and 100 kDa molecular weight cut-off Amicon Ultra Centrifugal Filters, and Lipofectamine 2000 reagent were obtained from Sigma-Aldrich (St. Louis, MO). Dimethyl sulfoxide (DMSO), triethylamine (TEA), and Paraformaldehyde (PFA) were obtained from Fisher BioReagents (Pittsburgh, PA). Ethylenediaminetetraacetic acid (EDTA) was procured from Quality Biological (Gaithersburg, MD). Protease inhibitor tablets, Dulbecco's Modified Eagle Medium (DMEM), Ethylenediamine tetraacetic acid (EDTA), and Pierce bicinchoninic acid (BCA) Protein Assay Kit were purchased from Thermo Fisher Pierce (Rockford, IL). qEV10 35 nm SEC columns were purchased from Izon Science (Medford, MA). CD63 Exo-Flow Capture Kit was purchased from System Bioscience (Palo Alto, CA). Optimal cutting temperature (OCT) Compound and enhanced green fluorescent protein (eGFP) mRNA were procured from Fisher Scientific. Cyanine5 (Cy5) NHS-ester was acquired from Lumiprobe (Cockeysville, MD). Zombie Red staining was obtained from BioLegend Way (San Diego, CA). Lastly, high-glucose Dulbecco's Modified Eagle's Medium (DMEM) without phenol red, penicillin–streptomycin antibiotic–antimycotic (PSA), and Opti-MEM were purchased from Gibco (Grand Island, NY).

2.2 Exosome harvest, modification, and characterization

Harvest of Exosomes. Exosomes (Exo) were harvested from non-fat bovine milk using our previously established protocol.[17] First, 18 mL of milk was diluted in 30 mL of PBS (pH 7.0) and centrifuged at 3000*g* for 15 min to pellet cells and cellular debris. The supernatant (17 mL) was then mixed with an equal volume of 0.25 M EDTA and incubated on ice for 15 min to chelate casein–calcium complexes and facilitate their removal. Next, the mixture underwent sequential one hour ultracentrifugation runs at 8000, 13 700, and 19 400 rpm; only the supernatant was transferred to subsequent runs. Exo were pelleted with a final run at 23 200 rpm for two hours and resuspended in 600 μL of PBS (pH 7.0). The resuspended Exo were then run through a 35 nm size exclusion chromatography (SEC) column and collected into ten fractions (5 mL each) for protein quantification *via* the bicinchoninic acid (BCA) assay. Fractions with the highest protein content were aliquoted with 5×10^{11} particles per tube in PBS and stored at −80 °C for future use.

Exosome modification. For modification with Avidin,[38,39] one tube of Exo (5×10^{11} particles) was first mixed with 25 μg of DSPE-PEG-biotin (3.31 nmol, 1.0 equiv.) in PBS and kept stirring for one hour at 37 °C (Fig. 2(A)). Excess DSPE-PEG-biotin was removed by using a 100 kDa MWCO centrifugal filter (4000 g, 20 min). Next, Texas Red-labeled Avidin (1.83 nmol, 0.55 equiv.) was added dropwise to the DSPE-PEG-biotin anchored Exo in 0.1 M sodium carbonate–bicarbonate buffer (pH 9.0) and stirred for 30 min at room temperature (RT). Unbound Avidin was filtered out using a 35 nm pore-sized SEC column and modified Exo were collected into twelve 500 μL fractions. The fraction with the highest modified Exo content was isolated based on Texas Red absorbance (585/611 Ex/Em) and protein content (BCA assay). These are referred to as Exo-Av.

For modification with CPC, 20 μg of DSPE-PEG-maleimide (5.88 nmol, 1.0 equiv.) was first mixed with 20 μg of Cy5-labeled CPC (5.55 nmol, 0.9 equiv.) in 100 μL of DMF overnight at RT. This reaction linked DSPE-PEG-maleimide with the cysteine on the C-terminus of CPC *via* click chemistry (Fig. 2(B)). Lyophilized DSPE-PEG-CPC was resuspended in 40 μL of DMSO and added dropwise to 1 tube of Exo (5×10^{11} particles) in 1 mL PBS while stirring continuously at 37 °C for 1 h. Unbound DSPE-PEG-CPC

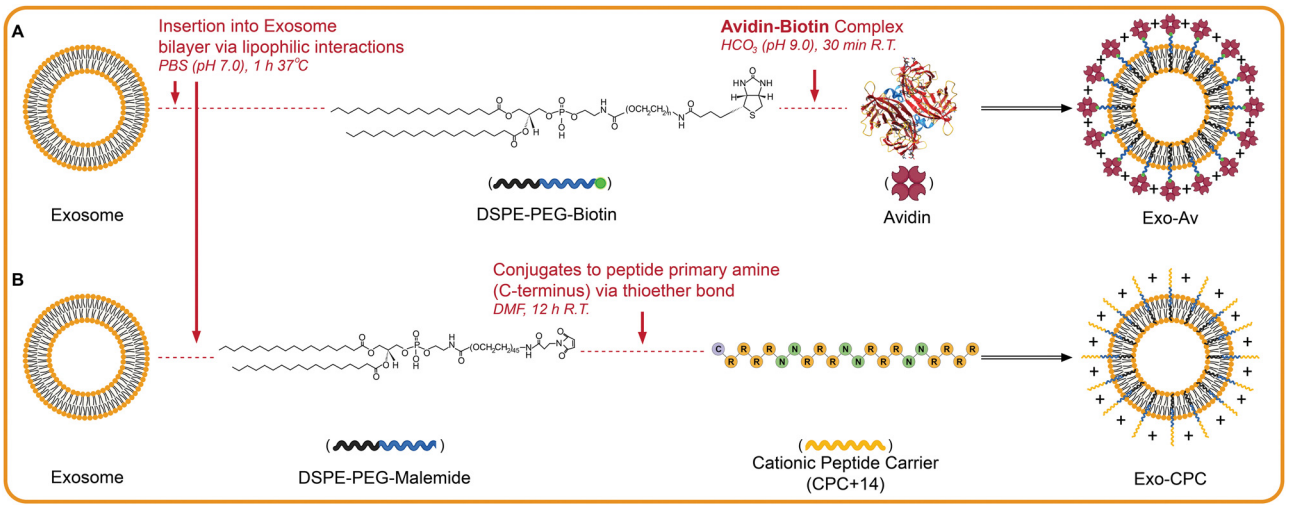

Fig. 2 Scheme illustrating anchoring of cationic motifs on exosome surface. (A) Exosome modification with avidin is achieved *via* insertion of DSPE-PEG-biotin into the lipid bilayer that is then linked *via* the avidin-biotin complex. (B) Exo modified with cationic peptide carriers of +14 net charge (CPC) are achieved *via* a similar insertion except it is DPSE-PEG-maleimide linked with CPC. The Maleimide end of the DSPE-PEG links to the cystine on the C-terminus of CPC *via* a thioether bond. Created with BioRender.com.

was filtered out using a 35 nm pore-sized SEC column and modified Exo were collected into twelve 500 μL fractions. Fractions were analyzed for Cy5 absorbance (617/685 Ex/Em) and protein content (BCA assay) to isolate the fraction with highest concentration of CPC-modified Exo. These are referred to as Exo-CPC.

Characterization of modified exosomes. Size and zeta potential (ζ) of cationic-motif-modified Exo (Fig. 3(A)) were measured in DI water using a Particle Analyzer (Litesizer 500, Anton Paar, Austria). The loading of cationic motifs on Exo surface was confirmed *via* flow cytometry, confocal microscopy, and transmission electron microscopy (TEM). Magnetic beads (9 μm in diameter, System Biosciences, Palo Alto, CA) were coated with CD63 antibodies following manufacturer's protocol; unconjugated antibodies were washed off. Approximately 7.5×10^{10} fluorescently labeled unmodified or cationic-motif-modified Exo were mixed with 100 μg CD63 coated beads. The mixture was stirred overnight at 4 °C and washed to remove any unbound Exo. The resulting mixture was run through a CytoFLEX SRT flow cytometer (Beckman Coulter, Brea, CA) to quantify the fluorescence events. At least 10 000 events were measured for each measurement. As additional confirmation, magnetic beads with captured Exo were imaged under 20× and 40× magnification using a ZEISS LSM 880 inverted confocal microscope (Carl Zeiss NTS Ltd, Oberkochen, Germany). Beads were imaged using FITC, Texas Red, and Cy5 channels as appropriate to confirm presence of modifications on Exo. Finally, unlabeled Exo were imaged using negative staining TEM to evaluate their morphology. Alcian blue was used for the mesh and uranyl acetate for Exo. Specifically, a grid was coated with 1% Alcian Blue to produce a positively charged surface and then Exo was added for adsorption. Finally, the grid was incubated with heavy metal salt uranyl acetate to negatively stain Exo and imaged.

2.3 Ocular tissue harvest and preparation

Cornea, lens, and vitreous humor harvest. Eyes of two-week-old male and female bovine were purchased from Research 87 Inc. (Boylston, MA) and transported in PBS for tissue dissection within two hours of animal sacrifice. First, all muscle and fatty tissue was removed, and a small incision was made circumferentially near the cornea. The incision was extended to separate the cornea and expose the lens. Corneas were stored in 95% glycerol and frozen at −80 °C to preserve their stromal structure.[40] Next, tweezers were used to remove the lens and separate the choroid from the retinal pigmented epithelium. The vitreous humor (VH) was then removed from the eyecup with the choroid attached to it. Finally, the choroid was removed and the vitreous harvested. The lens and VH tissues were frozen at −80 °C in 0.05 M NaCl.[34]

Retinal explant harvest. For retina studies, porcine eyes of two-month-old male and female pigs (Research 87 Inc., Boylston, MA) were used due to their lack of tapetum. The eye was cut along the mid frontal plane to expose the VH, which was carefully separated from the retina. The anterior eye cup was then placed in a Petri dish for 2–3 minutes with PBS until edges of the retina began detaching from the retinal pigmented epithelium (RPE). Then the retina was detached from the RPE using a spatula. Retinal explants were punched with a 5 mm biopsy punch and placed in a 6-well *trans*-well with low glucose DMEM media without phenol red and 1% PSA. 3 mL of media was placed in the lower compartment of the *trans*-well such that explants on the inner chamber remained nourished without being submerged.[41,42] All explants were handled using a transfer pipette to avoid damaging the tissue.

2.4 Transport of Exo through cornea

A clear poly(methyl methacrylate) chamber with two compartments (Fig. 4(A)) was used to measure the real-time one-dimensional transport of Exo as previously described.[43–45] In brief, the chamber compartments were first washed with 0.5% non-fat dried bovine milk to prevent non-specific binding. 6 mm diameter bovine corneal explant (~1.2 mm thick) was

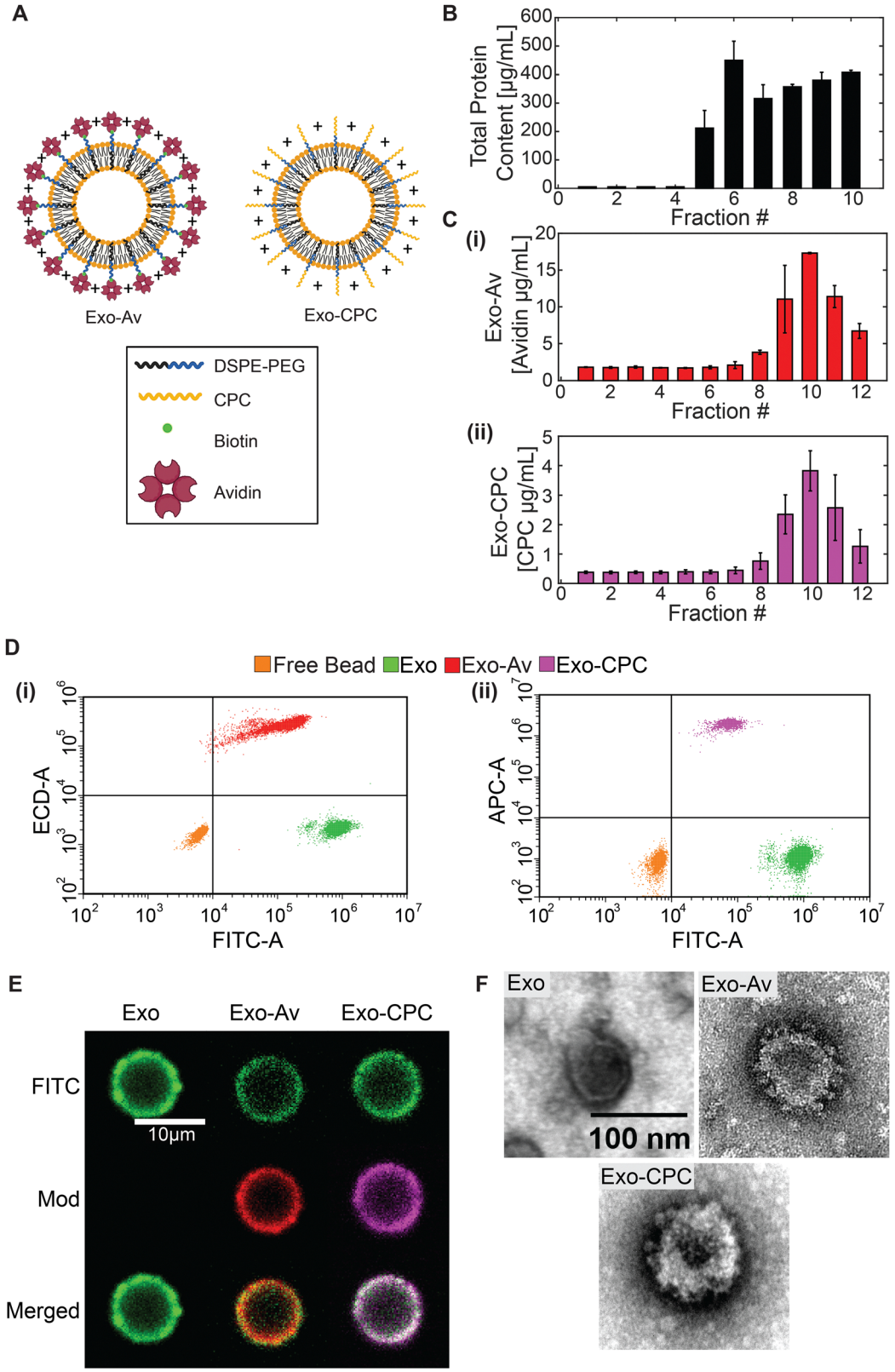

Fig. 3 (A) Diagram of surface modified Exo with cationic Avidin motifs (Exo-Av) and CPC (Exo-CPC). (B) Protein content after SEC isolation of Exo. (C) (i) Avidin (ii) CPC concentration per collected fraction after SEC purification of cationic-motif-modified Exo. (D) Flow cytometry of Exo modification. (i) FITC and Texas Red channels used for Exo-Av (ii) FITC and Cy5 channels used for Exo-CPC (E) Fluorescent images of magnetic beads used for flow cytometry. (F) TEM images of unmodified and cationic-motif-modified Exo.

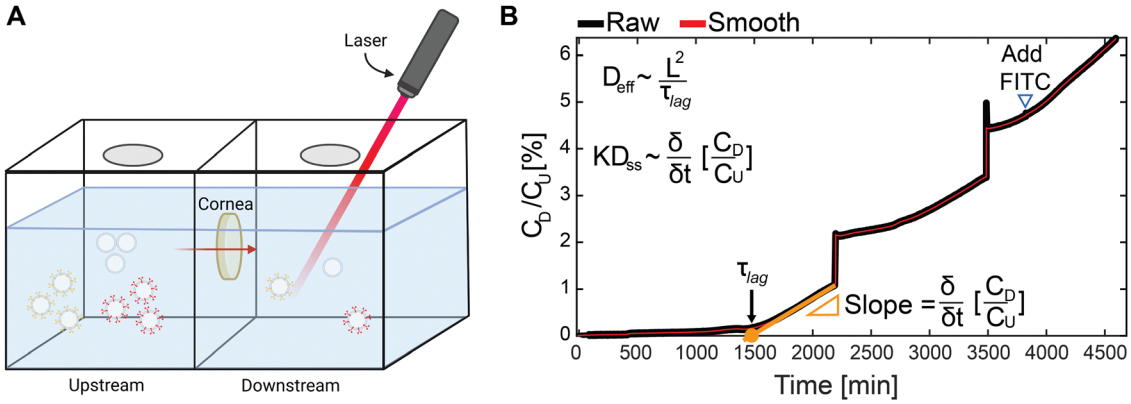

Fig. 4 (A) Diagram of transport chamber used for evaluating one dimensional transport of Exo through the corneal explants. Fluorescently labeled Exo were injected upstream, and the fluorescence downstream was monitored as particles moved through. (B) Representative transport curve from unmodified Exo. Downstream concentration (C_D) normalized by the upstream concentration (C_U) is plotted against time and monitored for when it reaches linearity. A parallel line is drawn at the linear region to obtain the x-intercept ($\tau_{\frac{1}{2}}$) and its slope which are then inputted into the corresponding equations to obtain the effective (D_{eff}) and steady state diffusion coefficients (KD_{ss}) where K is the partitioning factor.

held between the chambers. 2 mL of PBS supplemented with protease inhibitors (PBS-PI) was added to both compartments and kept at stirring to prevent any stagnation effects in the chamber. Once started ($t = 0$), 80 μg of FITC-labeled unmodified or cationic-motif-modified Exo (1 mg mL^{-1}) was injected in the upstream compartment. The Exo concentration in the downstream chamber was monitored continuously with a spectrofluorometer. To calibrate the downstream concentration, 20 μL from the upstream chamber was added to the downstream once the Exo concentration profile became linear. From the concentration profiles, effective diffusivity (D_{eff}) was estimated as:

$$D_{eff} = \frac{\delta^2}{6\tau_{lag}} \quad (1)$$

where δ is the tissue thickness and τ_{lag} is the time to achieve a steady state flux, which is estimated by using the x-intercept of the extrapolation of the linear slope of concentration *versus* time profile (Fig. 4(B)). The steady state diffusivity (D_{ss}) was approximated as:

$$KD_{ss} \sim \text{Slope} = \frac{\partial}{\partial t}\left[\frac{C_D}{C_U}\right] \quad (2)$$

where K is the Donnan partitioning factor, C_D is the downstream Exo concentration, and C_U is the upstream Exo concentration. K represents the sharp increase in the solute concentration at the tissue interface owing to internal electrical fields exerted by the negative fixed charge density of the tissue.[46,47]

2.5 Mechanical assessment of corneal explants and lenses

The bulk modulus (E_{eq}) and swelling pressure ($\Delta\beta$) of corneal explants and lenses were computed from load and displacement measurements collected with a TA ElectroForce 5500 Series dynamic mechanical analysis apparatus (TA Instruments, New Castle, DE) using a modified protocol from Warren *et al.*[48] Uniaxial, unconfined, stress relaxation testing was performed to remove transverse heterogeneity by allowing for radial transport of Exo and minimize loss from non-specific binding of cationic-motif-modified Exo to the porous membrane needed for confined testing. Bovine corneal explants (8 mm diameter, ~1.2 mm thick) were placed in a 15 mm diameter stainless steel well and compressed with a 10 mm diameter probe. Similarly, lenses (15 mm diameter, ~7 mm thickness) were placed in a 2 mL bath within a 22 mm diameter aluminum chamber with an accompanying 18 mm diameter plate probe. The loading regime consisted of at least three intermittent strain ramps and dwelling periods that applied stress on the tissue and then allowed it to relax.[48] Corneal explants were imposed a 0.08 N preload and equilibrated for 1100 s before its first stress-relaxation cycle. The first ramp applied 8% strain and all subsequent ramps applied 2% strain. While compressive stresses are represented by negative values, here we report the absolute value of the compressive strain. All dwelling periods held the strain for 1100 s. Cumulative strain did not exceed 16% to remain within the linear response of the cornea.[49,50] Lens tissues underwent the same protocol with a 0.05 N preload and 1000 s dwelling periods.

The stress and strain curves at each relaxation interval were fit to the standard linear solid model[48] to calculate the equilibrium stress (σ_{eq}) and characteristic time using non-linear least squares regression:

$$\sigma(t) = \sigma_{eq} + \left(\sigma \times e^{-\frac{t}{\tau}}\right) \quad (3)$$

where σ is the stress, t is time, and τ is the characteristic time constant. σ_{eq} was related to the strain (ε_0) through linear regression with the following Hooke's Law:

$$\sigma_{eq} = (E_{eq}(\bar{C}) \times \varepsilon_0) + \beta(\bar{C}) \quad (4)$$

where E_{eq} is the bulk modulus and β is the chemical stress (or the tissue free swelling stress generated by intra-tissue charge repulsions), which is equal to σ_{eq} at zero tissue strain ($\varepsilon_0 = 0$ in eqn (4)); both of these are a function of the salinity of the testing bath ($\bar{C}$).[48,51] Here the bulk modulus is a representation of the measurable tissue stiffness in triphasic framework.[49,51–53] Therefore, it is composed of a non-electrostatic (E_{eq}^{NE}, arising from support by the

solid macromolecular ECM) and electrostatic (E_{eq}^{E}, arising from like-charge repulsions within the tissue) component:[48]

$$E_{eq} = E_{eq}^{NE} + E_{eq}^{E} \quad (5)$$

To assess the impact of cationic-motif-modified-Exo on the bulk modulus and change in swelling pressures of the cornea and lens, tissues were incubated with unmodified Exo, Exo-Av or Exo-CPC (1.67 μg mL^{-1}) for one hour at RT.

Impact of charge shielding due to the uptake of modified Exo on the bulk moduli of cornea and lens was estimated using a charge shielding test as described previously.[48] Tissues were first equilibrated in a hypotonic bath solution (0.02 M NaCl) for 40 min at RT and then subjected to five stress-relaxation cycles. In between each cycle, the salinity of the bath was increased, and the tissue was allowed to equilibrate for the duration of a dwelling period. Then a reverse stress-relaxation cycle was performed (−6% and −2% strain for cornea and lens, respectively) to collect additional datapoints without exceeding the 16% strain limit. The tested concentrations were as follows: 0.05, 0.10, 0.19, 0.6, and 1.40 M NaCl. The bulk modulus measured at the highest bath salinity (1.40 M) can be attributed to non-electrostatic component (E_{eq}^{NE}) arising from the solid macromolecular ECM since all electrostatic interactions would be shielded at this high salinity. Since this non-electrostatic component of the bulk modulus, E_{eq}^{NE}, would not change with bath salinity and can be assumed to be constant, the electrostatic component (E_{eq}^{E}) that arises from like-charge repulsions within the tissue was estimated at each salinity by subtracting E_{eq}^{NE} from the total bulk modulus, E_{eq}. A theoretical estimation of the electrostatic component of the bulk modulus was computed using an ideal Donnan model previously described by our group,[51]

$$\pi_{FCD} = \Phi RT\left[\sqrt{\bar{C}_{FCD}{}^2 - 4C_0{}^2} - 2C_0\right] \quad (6)$$

where π_{FCD} is the change in swelling pressure within the tissue of given net fixed charge density (FCD), Φ is the osmotic coefficient for mobile ions withing the tissue (assumed to be 1 due to ideal osmotic behavior), R is the universal gas constant, T is the body temperature (310.15 K), C_{FCD} is the tissue' FCD, and C_0 is the concentration of NaCl in the external saline bath.[51] The FCD is defined as a function of tissue strain (ε):

$$\bar{C}_{FCD,eff} = \frac{\bar{C}_{FCD}}{(1-\varepsilon)} \quad (7)$$

Evaluating the swelling pressure at multiple strains (here 0.1 and 0.2) eqn (6) was used to theoretically predict the electrostatic component of the bulk modulus as:

$$E_{eq.}^{E,pred.} = \frac{d\pi_{FCD}}{d\varepsilon} \quad (8)$$

Bulk modulus predictions were computed using the estimated electrostatic component (eqn (8)) and the measured non-electrostatic component (Table 3).

Swelling pressure measurements following treatment with unmodified and cationic-motif-modified Exo. To assess the impact of cationic-motif-modified Exo on the swelling stress of the tissues, explants were subjected to three stress-relaxation cycles at 0.15 M and 1.40 M NaCl bath concentrations following treatment with unmodified and cationic-motif-modified Exo as detailed above. The change in swelling pressure was defined as:

$$\Delta\beta = \beta(\bar{C}_{0.15M}) - \beta(\bar{C}_{1.4M}) \quad (9)$$

2.6 Transport studies through the vitreous humor

Fluorescence recovery after photobleaching (FRAP). 20 μL of 1×10^{11} FITC-labeled Exo were injected superficially in the center of the slide wells containing 400 μL of PBS, healthy VH, or GAG-depleted VH. The slides were incubated for one hour at 4 °C in a 100% humidity to allow for homogenization through passive diffusion. FRAP measurements were made in 50 × 50 μm randomly selected regions by using a confocal microscope (ZEISS LSM 880) equipped with a 40× water immersion magnification objective. As a control, 5 kDa and 500 kDa FITC-labeled dextrans were also characterized. The resulting fluorescence curves (Fig. 6(A)) were fitted to:

$$f = \sum_{n=1}^{\infty} \frac{(-\kappa)^n}{n!} \cdot \frac{1}{1 + n\left[1 + 2\frac{t}{\tau_{\frac{1}{2}}}\right]} \quad (10)$$

where t is the time in seconds, $\tau_{1/2}$ is the characteristic diffusion time, and κ represents the depth of bleaching calculated as:

$$\frac{(1 - e^{-\kappa})}{\kappa} = \frac{F_i}{F_0} \quad (11)$$

where F_i and F_0 are the fluorescence before and right after photobleaching, respectively. The $\tau_{1/2}$ is defined as the time when the curve reaches 50% of its final fluorescence, F_∞. From the fitted curve, the mobile fraction (M_f) was computed as the ratio between the final and initial fluorescence relative to the fluorescence right after photobleaching:

$$M_f = \frac{F_\infty - F_0}{F_i - F_0} \quad (12)$$

and the effective diffusivity coefficient was approximated as:

$$D_{eff} = \frac{\omega^2}{4\tau} \quad (13)$$

where ω is the width of the Gaussian beam of the laser, the e^{-2} halfwidth.[17,36]

Lastly, the particle population flux was approximated as the average diffusivity (P_A), to better understand how the entire particle population travels through the VH.[36] FRAP only considers mobile particles when computing the diffusivity coefficient so by ignoring the immobilized particles it assumes that they will remain trapped indefinitely. Therefore, P_A provides an approximation of the diffusion of the entire population through the tissue by averaging the diffusivity of mobile and immobile particles, and is defined as:

$$P_A = M_f \times D_{eff} \quad (14)$$

GAG-depletion of the vitreous humor. To simulate VH with extensive liquefaction or synchysis, freshly harvested bovine VH underwent sequential chondroitin sulfate (CS)-GAGs and

hyaluronic acid (HA) digestion. First, VH was mixed with 0.05 units per mL chondroitinase ABC (ChABC) in tris–HCl buffer (pH 8.0) and incubated at 37 °C for six hours while shaking. ChABC activity was quenched by transferring the tissue samples to PBS-PI. For HA digestion, tissue samples were incubated in 110 units of hyaluronidase dissolved in 100 mM sodium acetate buffer (pH 5.7, 77 mM NaCl, 0.01% BSA) for 48 hours at 37 °C. Hyaluronidase activity was quenched by using PBS-PI. 1,9-Dimethylmethylene blue (DMMB) assay was used to quantify the loss of CS-GAGs.[54] HA loss was estimated by quantifying water loss.[30]

Microscale thermophoresis (MST). The binding affinity of unmodified and cationic-motif-modified Exo with HA was quantified using MST. To prevent aggregation and binding to the capillary walls, MST buffer consisting of PBS, Tween 20, and Sodium dodecyl sulfate (SDS) (0.1% 0.01 μM Tween 20, 0.05% 1 μM SDS) was used.[55] Solutions of MST buffer with increasing concentration of HA were prepared and an equal volume of FITC-labeled Exo was added such that approximately 1×10^{10} particles were present per 20 μL of solution. Solutions were then incubated for 15 min at RT before collecting in glass capillaries for MST testing. A concentration range between 3.0×10^{-5} and 3 μM of HA ligand was selected. Finally, the responses were fit to the Hill–Langmuir equation,

$$\theta = \frac{[L]^n}{K_d^n + [L]^n} \quad (15)$$

where θ is the fraction bound, L is the HA ligand concentration, n is the Hill coefficient, and K_d is the binding affinity defined as the concentration of L at which 50% of the ligand is bound.

2.7 Delivery of mRNA to the retina

Transport through the retina. To assess transport through retina, retinal explants with an intact inner limiting membrane (ILM) were prepared as described in Section 2.3 and incubated for 24 hours (37 °C, 5% CO_2) with a 1–2 μL droplet of Cy5-labeled Exo (0.25–0.5 μg μL^{-1}) placed on its ILM. The droplet volume and concentration were chosen to avoid submerging the explant and limit the transport of Exo to one dimension while maximizing particle count. A free Cy5 dye control was tested to account for any dye that may detach from the Exo. After incubation, tissues were washed with PBS and fixed with 4% PFA. Tissues were stained with DAPI, cryoprotected overnight, and frozen in Optimal Cutting Temperature (OCT) Compound, and then cryo-sectioned in 12 μm-thick slices for imaging (Zeiss Axio Observer Inverted Widefield). Cy5 signal was quantified across the thickness of the tissue.

Exosome mRNA loading and transfection. Exo were loaded with eGFP mRNA using previously described protocols.[17,36] 7.5 μL of lipofectamine 2000 (1 mg mL^{-1}) and 1.5 μL of eGFP mRNA (1 mg mL^{-1}) were suspended in 75 μL of OptiMEM each to obtain lipoplexes. Exo (167 μg) were added dropwise to the lipoplexes and left shaking at 37 °C for 30 min. After incubation, RNase-A (4.3 μL) was added to the Exo-mRNA solution and was left shaking for 30 min at 37 °C to cleave unloaded mRNA. Finally, loaded Exo were purified after three centrifugation rounds (3000*g*, 15 min). For loaded Exo-CPC, only one centrifugation round was performed to minimize aggregation. Retinal explants were then incubated with 20 μL droplets of Exo (0.33 μg μL^{-1}) to maximize transfection. An equivalent load of mRNA was delivered using lipofectamine lipoplexes as positive control. GFP fluorescence was summed across the tissue for quantification.

Retinal tissue viability. Retinal explants incubated with Exo for 24 hours were stained with Calbryte AM and Zombie Red, fixed, and cryosectioned. Freshly harvested tissues were stained immediately to be used as a positive control and tissues incubated in 10% DMSO media were used as a negative control. Explants incubated in PBS for 24 hours were used as controls to account for any harm due to tissue handling. Calbryte AM fluorescence was quantified to estimate the viability of the retinas relative to positive and negative controls.

2.8 Statistical analysis

The data are reported as mean ± standard deviation. All characterization and transport experiments used N = 4–6 independent repeats. All mechanical analysis and retinal explant experiments used N = 3–4 repeats. Experimental groups were compared using one-way analysis of variance (ANOVA) and *post hoc* Tukey's honestly significant difference (Tukey's HSD) test. Statistical significance was defined as p values below 0.05.

3 Results

3.1 Exosome harvest, modification, and characterization

Fractions 5–7 from the Exo purification were expected to contain high purity Exo, 3×10^9 particles per μg, within the desired size range, 60–200 nm, according to previous work by our group.[17,36] Fraction 6 was selected for further experiments because it measured the highest protein content (450 ± 67 μg mL^{-1}), indicating the highest content of Exo (Fig. 3(B)). Fraction 10 of the SEC-separated Exo modified with Avidin-Texas Red (Exo-Av) showed the highest Texas Red and protein content, demonstrating presence of Exo-Av (Fig. 3(C)-(i)). Similarly, fraction 10 of the SEC-separated Exo modified with CPC (Exo-CPC) presented the highest Cy5 signal and protein content (Fig. 3(C)-(ii)). The molar equivalent ratio of Avidin and CPC per Exo was estimated to be 600 : 1 and 450 : 1, respectively, based on the absorbance and protein measurements from fraction 10 of each group (Table 1). The use of Avidin motifs increased the mean ζ-potential values of Exo from −22.3 mV to −6.6 mV and to −2.0 mV for Exo-CPC (Table 1). These increments represent a near complete shielding of the anionic surface charge of Exo.

The strong FITC signal from unmodified Exo formulations from the flow cytometry data indicated successful binding of Exo to the CD63 antibodies on magnetic beads (green, Fig. 3(D)). Exo-Av (red, Fig. 3(D)-(i)) demonstrated both Texas Red of Avidin and FITC signal of unmodified Exo, and Exo-CPC (purple, Fig. 3(D)-(ii)) exhibited both Cy5 of CPC and FITC of unmodified Exo confirming successful surface modifications. Confocal images of the magnetic beads displayed dual

Table 1 Characterization of cationic Exo. The molar equivalent ratio of Exo to loaded motif, properties of the motif, size, polydispersity index (PDI), and surface charge of all exosome formulations

	Ratio Exo to Motif loading	Motif configuration (molecular weight [kDa])/net charge	Size [nm]	PDI [%]	Surface charge [mV]
Exo	—	—	192 ± 38	21.6 ± 7.7	−22.3 ± 2.8
Exo-Av	1:600	Four identical subunits (66)/+6 to +20	257 ± 36	23.3 ± 8.6	−6.6 ± 4.3
Exo-CPC	1:450	$RRRR(NNRRR)_3R$ (2.99)/+14	237 ± 39	22.5 ± 7.9	−2.0 ± 0.8

fluorescence of both the Exo and the surface anchoring further corroborating the findings of the flow cytometric analysis (Fig. 3(E)). Finally, TEM imaging revealed that Exo morphology was not affected post modification (Fig. 3(F)).

3.2 Transport of Exo through cornea

Unmodified Exo demonstrated 2.8-fold and 4.4-fold higher effective diffusivity (D_{eff}) than that of Exo-Av and Exo-CPC, respectively, due to a lack of electrostatic binding interactions with the anionic constituents of the tissue (Fig. 4 and Table 2). Once steady state was achieved, Exo-CPC displayed the highest steady state diffusivity (KD_{ss}), about 1.6-fold faster than unmodified Exo and 2.3-fold faster than Exo-Av. A contributing factor to this trend is the coulombic attractive forces between the anchored CPC motifs and the negative FCD of the cornea that owing to charge-based Donnan effects[46,48] can enhance both the concentration and the rate of transport of cationic solutes into the anionic tissue.[46,47] The Donnan partitioning factor, K, was defined as 1 for unmodified Exo as they have no attractive coulombic interactions within the matrix of the cornea; assuming that the steady state diffusivity, D_{ss} is constant for all Exo formulations due to their similar sizes (Table 1), K for cationic-motif-modified Exo can be estimated by taking ratios of their respective KD_{ss} (Table 2). K for Exo-CPC measured greater than 1 ($K \sim 1.6$) implying that its concentration at the tissue interface would partition up by a factor of 1.6, which would enhance its flux into the tissue compared to unmodified Exo. Similarly, K for Exo-Av was measured to be less than 1 ($K \sim 0.7$) implying that its uptake could not achieve equilibrium potentially owing to aggregation issues (observed experimentally) that could hinder its intra-tissue transport.[56] Free FITC diffused as expected given its small size and hydrophilicity.[43,57,58]

3.3 Electro-mechano-chemical effects of modified Exo on corneal explants and lenses

Exposure to cationic-motif-modified Exo was found to minimally impact the total bulk modulus (E_{eq}) of both tissues. There were no significant changes in stiffness of either tissue after one hour incubation with any of the Exo formulations (Fig. 5(A)-(i), (ii)). Increasing bath salinities reduced the bulk moduli of both tissues (Fig. 5(C)). The lens response followed the ideal Donnan Model prediction (black line, R^2 = 0.91, Fig. 5(C)-(ii)) closely, but the cornea displayed a weak fit (R^2 = 0.42, Fig. 5(C)-(i)) which could be attributed to differences in their composition. Corneal stroma is two orders of magnitude thicker than the lens capsule (500 *vs.* 3.5 μm) and nearly 30% of its dry weight is composed of GAGs, which plays a key role in maintaining the laminar organization of the stroma.[33,59–62] The corneal stroma, therefore, is more sensitive to counterion condensation and the subsequent changes to collagen fibril organization explaining the poor fit with the ideal Donnan Model values (ESI,† Fig. S1).[48,63,64] At physiological salinity (~0.15 M), the electrostatic component accounted for 68% and 52% of the bulk modulus in cornea and lens, respectively (Table 3).

The change in swelling pressure showed no significant difference between experimental and control groups for either tissue (Fig. 5(D)-(i), (ii) and Table 3). Corneal explants incubated in Exo-Av showed a drop of 150 Pa in swelling pressure compared to the PBS control while the Exo-CPC-incubated lenses showed a drop of 100 Pa. This close to 30% reduction in corneal swelling pressure is within the normal physiological range and may result in ~10% decrease in stromal thickness.[65,66] The corneal endothelial layer can counteract this tissue deswelling by modulating metabolic activity to allow for more water to transport into the tissue.[67,68]

3.4 Transport studies through vitreous humor

Fluorescence recovery after photobleaching (FRAP) Analysis. Exo formulations in PBS presented no significant differences in their effective diffusivities (D_{eff}) or the mobile fraction (M_f) due to their comparable size (Fig. 6(B), and Table 4). Their M_f was approximately 1 meaning that the transport of the entirety of the population in the PBS buffer was unhindered. Accordingly, the average diffusivity (P_A) followed the same trend as the D_{eff} (Table 4). 5 kDa and 500 kDa FITC-labeled dextrans measured diffusivities comparable to that reported in literature (Fig. 6(B) and Table 4).[69,70] FRAP measurements were also conducted in healthy and GAG-depleted VH. The GAG-depleted VH had a 63% loss in chondroitin sulfate (CS) concentration and a 42% loss in water content (Fig. 6(C)). Water content was used as an indirect measurement of HA content, which was approximated to be 60% based on previous reports.[30] GAG loss between 50% and 67% was targeted in order to simulate synchysis senilis observed in individuals over 80 years old.[32,71]

In healthy VH, cationic-motif-modified Exo exhibited 1.5-fold faster mean D_{eff} than that of unmodified Exo potentially

Table 2 Corneal explant transport. Effective (D_{eff}) and steady state diffusivities (KD_{ss}) of free FITC dye control and exosome formulations. Donnan partitioning factor (K) was estimated for unmodified Exo, Exo-Av, and Exo-CPC

	D_{eff} [$\times 10^{-7}$ cm^2 s^{-1}]	KD_{ss} [$\times 10^{-4}$ cm^2 s^{-1}]	K
FITC	1.00 ± 0.13	0.39 ± 0.16	—
Exo	0.31 ± 0.11	0.99 ± 0.23	1
Exo-Av	0.19 ± 0.10	0.70 ± 0.24	0.7
Exo-CPC	0.07 ± 0.01	1.63 ± 0.16	1.63

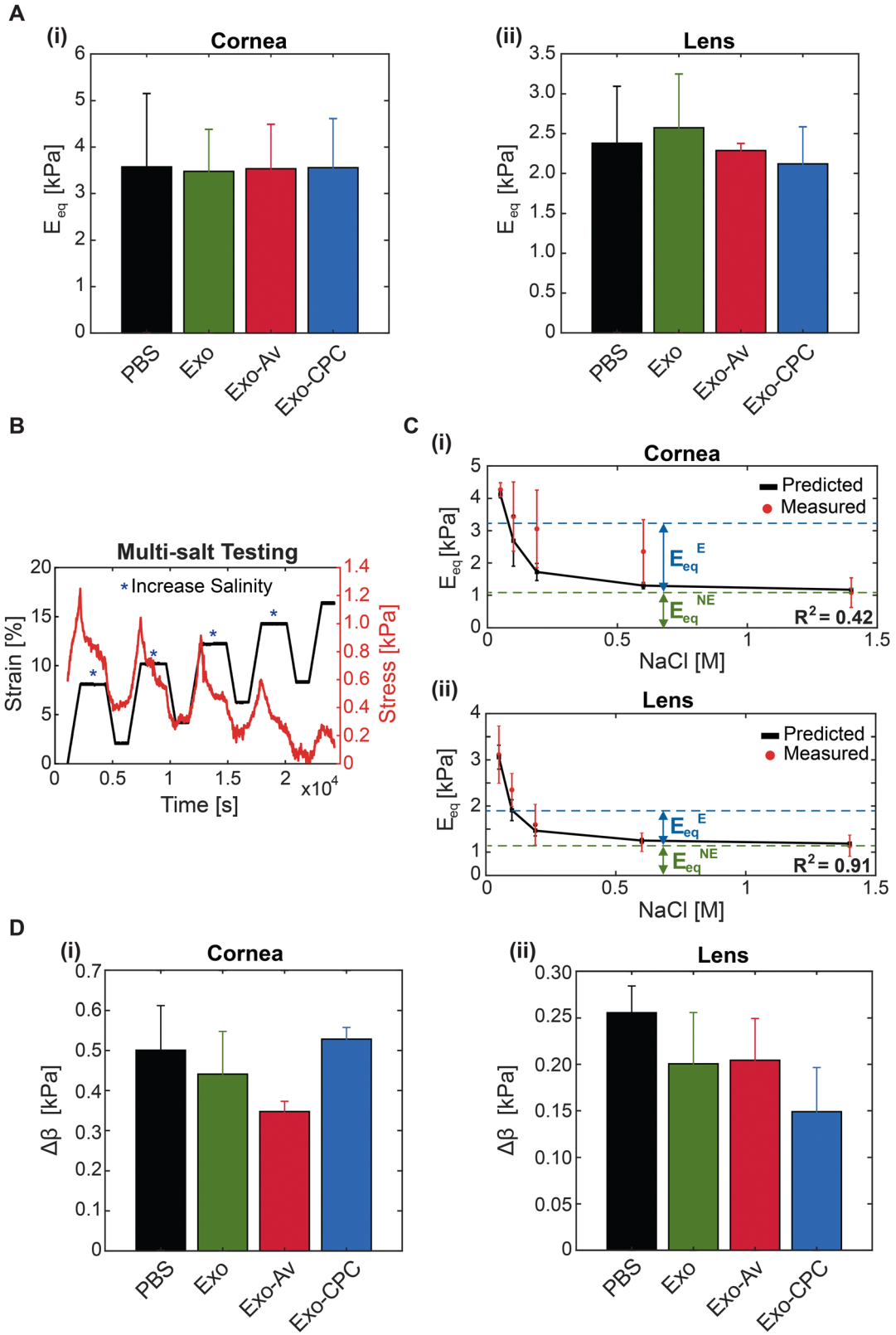

Fig. 5 (A) Measured bulk modulus from (i) corneal explants (ii) and lenses after one hour incubation in PBS, unmodified or cationic-motif-modified Exo. (B) Representative stress and strain vs time plot of multi-salt experiment. Testing bath salinity was increased at every timepoint indicated by the asterisk. (C) Measured (red) and predicted (black) bulk modulus (E_{Eq}) *vs.* bath salinity. (i) corneal explants and (ii) lenses. Non-electrostatic (E_{Eq}^{NE}, green) and electrostatic (E_{eq}^{E}, blue) components of the bulk modulus are highlighted with dashed lines. (D) Change in chemical stress measured in (i) corneal explants and (ii) lenses incubated for one hour in PBS, unmodified or cationic-motif-modified Exo.

Table 3 Non-electrostatic (E_{eq}^{NE}) and electrostatic (E_{eq}^{E}) components of the bulk modulus at different saline bath concentrations from corneal explants and lenses after one hour incubation with Exo at room temperature

Saline bath [M]	Cornea		Lens	
	E_{eq}^{NE} [kPa]	E_{eq}^{E} [kPa]	E_{eq}^{NE} [kPa]	E_{eq}^{E} [kPa]
0.05		3.19 ± 0.27		1.97 ± 0.39
0.10		2.35 ± 0.62		1.21 ± 0.17
0.15	1.08 ± 0.45	1.93 ± 0.81	1.14 ± 0.23	0.46 ± 0.23
0.60		1.32 ± 0.47		0.08 ± 0.07
1.4		0		0

owing to the presence of transport enhancing hydrophilic PEGs (Fig. 6(D)-(i), (ii) and Table 4). Cationic-motif-modified Exo exhibited 4-fold lower mean M_f owing to charge-based binding with the VH GAGs (Fig. 6(D)-(i) and Table 4). It should be noted that FRAP only considers mobile particles when computing the effective diffusivity coefficients. To estimate the transport flux of the entire particle population, we introduced an average diffusivity parameter ($P_A = M_f \times D_{eff}$), which averages the diffusivity of both mobile and immobile particles.[36] While the D_{eff} of unmodified Exo measured slower than that of cationic-motif-modified Exo, P_A indicated that unmodified Exo would diffuse 3-fold faster in VH owing to its larger mobile fraction (M_f, Exo: 0.65; Exo-Av: 0.15; Exo-CPC: 0.15). These data highlight the competing effects of charge-induced hindrance and hydrophilic PEG-induced enhancement on particle transport. In younger patient population, with little to no vitreous liquefaction, the slower moving cationic-motif-modified Exo can be used to create intravitreal drug depots and provide sustained drug release.

In GAG-depleted VH, all Exo formulations exhibited lower D_{eff} compared to that in the healthy VH (0.70×, 0.91×, and 0.76× for Exo, Exo-Av, and Exo-CPC, respectively). The reduction was likely due to the loss of water content following GAG depletion which, in *ex vivo* tissue, reduces the distance between collagen fibrils thereby decreasing the tissue mesh size.[30,72] *In vivo*, the volume of the VH remains relatively constant despite collagen and GAG degradation, which would instead increase the tissue mesh size.[32,72] Cationic-motif-modified Exo presented a 1.75-fold faster D_{eff} than the unmodified Exo and close to 100% mobility in GAG-depleted VH (Fig. 6(D)-(ii) and Table 4). Reinforcing these trends, P_A indicated cationic-motif-modified Exo had a 2.3-fold higher diffusivity than unmodified Exo (Table 4). The enhanced mobility and transport rate of cationic-motif-modified Exo in GAG-depleted VH can be attributed to the reduced charge-based binding interactions owing to depletion of GAGs as well as the presence of hydrophilic PEGs that are known to enhance macromolecule transport in the VH.[30,31] Therefore, in older patients with severe vitreous degeneration, the cationic-motif-modified Exo would transport rapidly across the vitreous to reach and target the retinal cells.

MST analysis. Unmodified Exo exhibited the lowest binding affinity with the vitreous HA compared to the cationic-motif-modified Exo due to their negatively charged surface (green dashed, Fig. 6(E) and Table 5). Exo-Av and Exo-CPC measured 4.3-fold and 2-fold smaller K_d values than the unmodified Exo, respectively, implying stronger binding with HA due to electrostatic binding (red and blue dashed, Fig. 6(E) and Table 5). Only Exo-Av indicated co-operative binding with HA (Hill Coefficient, n = 1.92), likely due to a higher density of available binding sites; Exo-Av has a higher molar ratio of anchored cationic motifs compared to Exo-CPC. Additionally, Avidin is a globular protein with 22× higher MW compared to CPC offering larger surface area for electrostatic binding interactions.

3.5 Retinal transport, viability, and transfection

Retinal transport. Fluorescent images of the retinal cross-section indicated a larger presence of unmodified Exo and Exo-CPC in the inner limiting membrane and ganglion cell layer (GCL) (Fig. 7(A)-(i)). However, Exo-CPC had a signal 20-fold stronger along the GCL (Fig. 7(A)-(ii)). Fluorescence quantification revealed that Exo-CPC transported through the outer nuclear layer (ONL) at a quantity 10-fold higher than unmodified Exo (Fig. 7(A)-(ii)). The superior penetration rate of Exo-CPC can be attributed to the presence of cationic motifs that created a Donnan partitioning factor larger than one, which increased the concentration of Exo-CPC at the surface of the retina similar to what we observed in the cornea (Table 2). Additionally, the density of heparin sulfate and CS-GAGs increases from the ILM to ONL providing greater binding site density and facilitating deeper penetration for Exo-CPC (Fig. 7(A)-(ii)).[73] Free Cy5 dye alone was undetectable along the retinal cross-section.

Retinal transfection. Unmodified Exo showed the weakest signal, and GFP fluorescence was primarily observed near the ganglion cell layer (Fig. 7(B)-(i)). Exo-CPC showed fluorescent signaling across all retinal layers, but its strongest localization was in the ONL similar to Lipofectamine 2000 (Fig. 7(B)-(i)). Although these localizations are not indicative of their penetration depth, these observations support that the superior transport of Exo-CPC (Fig. 7(A)) facilitates targeting of dense regions within the retina like the ONL. Quantifying the total fluorescence across the retinal layers revealed that Exo-CPC was 2.8 times more effective compared to unmodified Exo (Fig. 7(B)-(ii)). Yet again Exo-CPC benefits from the presence of cationic motifs, which are likely triggering endocytosis and micropinocytosis pathways by increasing the contact time with negatively charged cell walls.[74–79]

Retinal viability. Live/dead staining of unmodified Exo and Exo-CPC-treated retinas revealed nominal differences compared to the 24-hour control (Fig. 7(C)-(i)) and no change to the tissue viability (Fig. 7(C)-(ii)). These results were expected as extensive work has established the safety of Exo[80–82] and our group has demonstrated the safety of using CPC for chondrocyte targeting.[74,83,84] Positive and negative controls behaved as expected (ESI,† Fig. S2).

4 Discussion

In this study we established the potential of cationic-motif-modified milk-derived exosomes for targeted delivery of mRNA to retinal photoreceptors *via* the topical route. We designed two

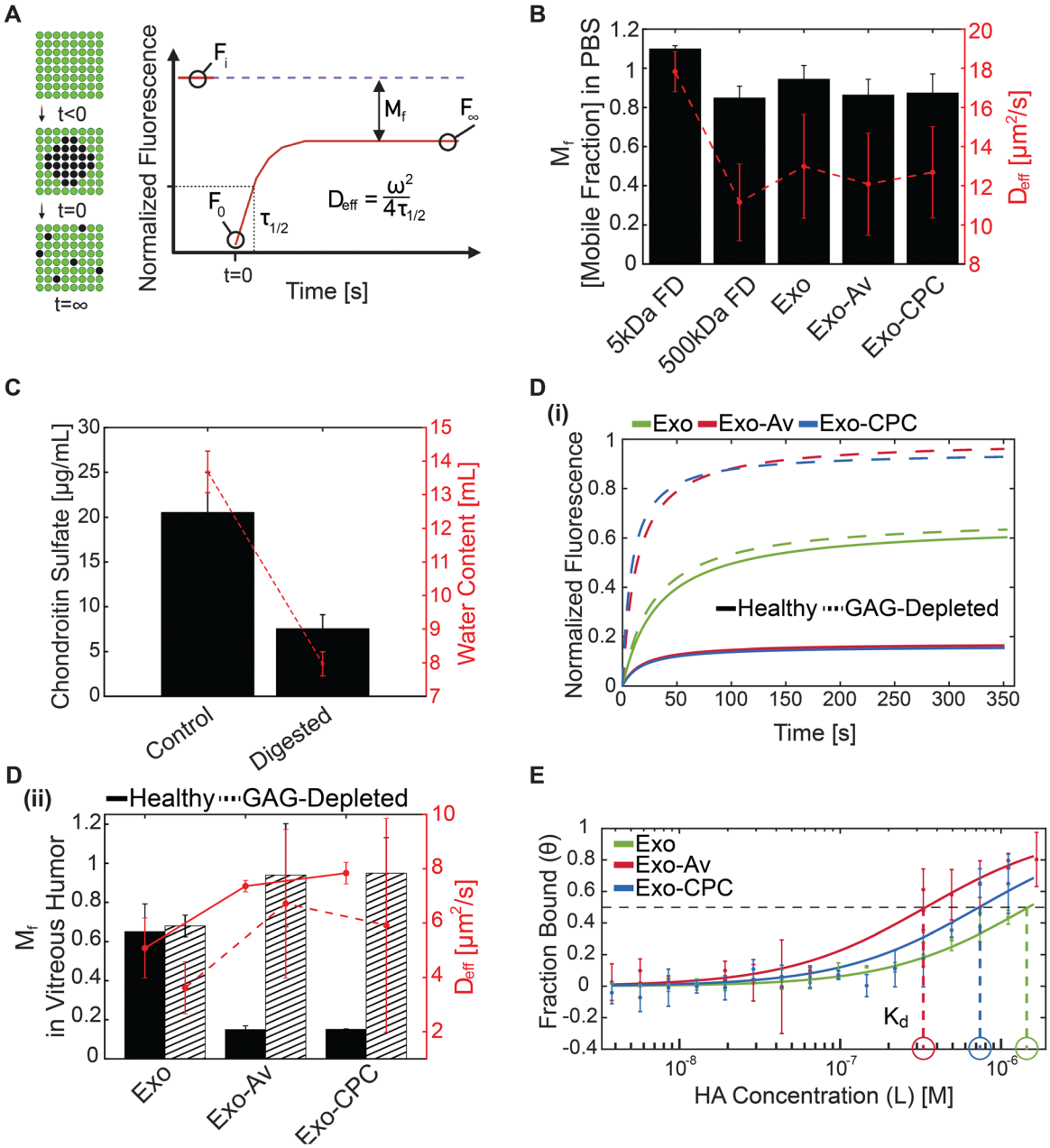

Fig. 6 (A) Representative curve and key parameters of FRAP. (B) Mobile fraction (M_f) and effective diffusion coefficient (D_{eff}) measured from FRAP in PBS for 5 and 500 kDa FITC-labeled dextrans (FD), unmodified Exo, Exo-Av, and Exo-CPC. (C) Chondroitin sulfate concentration and water content of healthy and GAG-depleted vitreous. (D) FRAP results from exosome transport in healthy and GAG-depleted vitreous humor. (i) Representative curves from unmodified and cationic-motif-modified Exo in healthy (solid) and GAG-depleted vitreous (dashed). (ii) M_f and D_{eff} of Exo in healthy (solid) and GAG-depleted (dashed) vitreous. (E) Micro-thermophoresis curves showing fraction of unmodified Exo, Exo-Av, and Exo-CPC bound to increasing concentrations of hyaluronic acid (HA). Binding affinity (K_d, circles) are highlighted.

exosome formulations (Exo-Av and Exo-CPC) by anchoring a basic glycoprotein Avidin and an arginine-rich cationic peptide carrier with a net charge of +14 *via* PEG lipid insertion onto milk-derived exosomes without affecting their size or morphology (Fig. 2, 3(F) and Table 1). Our lab has previously designed Avidin and CPC-based nanocarriers for targeted drug delivery to other negatively charged tissues including cartilage,[39,54,74] intervertebral discs[85] and mucin,[17,36] and for diagnostic imaging applications.[86] Here, cationic and PEG motifs were anchored in sufficient density to enable a near complete shielding of the anionic surface charge of exosomes while making them hydrophilic (Table 1). This allowed them to take advantage of weak-reversible ionic binding interactions with the anionic GAGs and water content in various ocular tissue compartments including the cornea, vitreous humor (VH), and the retina that enhanced their intra-tissue transport and binding properties. Our work shows that owing to the presence of cationic motifs on exosomes, their steady state diffusivity through the cornea was

Table 4 FRAP measurements of effective diffusivity (D_{eff}) of Exo, mobile fraction (M_f), and average diffusion (P_A). Baseline values were obtained in PBS for 5 kDa and 500 kDa FITC-labeled dextrans (FD), unmodified Exo, Exo-Av, and Exo-CPC

	PBS			Healthy VH			GAG-depleted VH		
	D_{eff} [$\mu m^2\ s^{-1}$]	M_f	P_A [$\mu m^2\ s^{-1}$]	D_{eff} [$\mu m^2\ s^{-1}$]	M_f	P_A [$\mu m^2\ s^{-1}$]	D_{eff} [$\mu m^2\ s^{-1}$]	M_f	P_A [$\mu m^2\ s^{-1}$]
5 kDa FD	17.8 ± 1.0	1.0	17.8	—	—	—	—	—	—
500 kDa FD	11.2 ± 2.0	0.85	9.5	—	—	—	—	—	—
Exo	13.0 ± 2.7	0.95	12.3	5.1 ± 1.1	0.65	3.3	3.6 ± 1.0	0.68	2.5
Exo-Av	12.1 ± 2.6	0.86	10.4	7.4 ± 0.2	0.15	1.1	6.7 ± 2.7	0.94	6.3
Exo-CPC	12.7 ± 2.3	0.88	11.1	7.8 ± 0.4	0.15	1.2	5.9 ± 3.9	0.94	5.6

Table 5 Binding affinity of exosome formulations with hyaluronic acid (HA). Micro-thermophoresis data was fit to the Hill–Langmuir equation to obtain the binding affinity (K_d) and the Michaels–Menten equation to obtain the Hill coefficient (n)

	K_d [μM]	Hill coefficient
Exo	1.48 ± 0.83	1.04
Exo-Av	0.34 ± 0.14	1.92
Exo-CPC	0.73 ± 0.15	0.90

enhanced by 2-fold compared to unmodified exosomes (Table 2). Our FRAP results confirm that milk exosomes with a size range of 60–200 nm can transport through the VH without steric hindrance (Fig. 6(D)-(ii)). In the retina, cationic-motif-modified exosome, Exo-CPC penetrated through the full thickness of the tissue, from ganglion cell layer (GCL) to the outer nuclear layer (ONL), by taking advantage of charge-based binding interactions with the tissue GAGs that resulted in a 20- and a 10-fold higher uptake in GCL and the deep ONL layers, respectively, compared to unmodified exosomes (Fig. 7(A)). Cationic motifs also increased the contact time of Exo-CPC with the anionic cell lipid bilayer enhancing their mRNA transfection efficiency by 3-fold compared to unmodified exosomes (Fig. 7(B)-(i), (ii)). Finally, cationic-motif-modified exosomes did not adversely impact the electro-mechano-chemical homeostasis in cornea or the lens and elicited no cytotoxic effect on retinal cells (Fig. 7(C)-(i), (ii)). Cationic-motif-modified exosomes, therefore, offer themselves as a nanocarrier platform system for drug and gene delivery to retinal photoreceptors potentially *via* the topical route.

The eye presents several pharmacokinetic barriers for the treatment of vitreoretinal diseases *via* the topical delivery (Fig. 1). While invasive methods like intraocular injections can bypass some of these barriers, they are associated with patient discomfort and increasing risks of errors and infections when used repeatedly. Topical delivery to target the back of the eye is desirable but currently not feasible since 95–99% of drugs lose their bioavailability at the cornea following topical application as they get flushed into the circulation by the tear film. Therapeutics must penetrate the 20 nm intercellular junction of the corneal epithelium or move intracellularly quickly. We show that when Exo-CPC contacts the corneal surface, the cationic motifs facilitate electrostatic binding interactions at a microscopic scale with anionic GAGs in the corneal stroma resulting in partitioning up of Exo-CPC concentration by a Donnan factor, K of 1.6 that enhances its initial rate of transport and its steady state diffusivity by 2-fold compared to unmodified exosomes. Previous studies using rabbits have shown that topically applied cationic lipids loaded with acyclovir result in 2–4-fold higher bioavailability in cornea compared to free drug or anionic lipids despite 2–4-fold slower permeability through the cornea.[24] This charge-based surface binding combined with enhanced flux can help exosomes to cling onto the corneal surface which would prevent their clearance and facilitate efficient transport through the cornea for topical applications.[24] Additionally, the presence of PEGs eases Exo-CPC diffusion through the stroma by minimizing hydrophobic trapping within collagen pockets.[25] Exo-Av suffered from aggregation issues resulting in lower partitioning of $K = 0.7$; further optimization of the formulation by changing the extent of avidin functionalization and use of surfactants like Tween 20 can reduce ionic crosslinking induced aggregation issues.[17] Our SEC-purified exosomes have a controlled size range with low polydispersity index (Table 1) and thus can also circumvent getting trapped within the lens capsule with a 20 nm pore size.[26]

The next significant ocular barrier is the VH wherein the solute diffusion is primarily governed by hydrophobic interactions with collagen fibers and electrostatic binding interactions with its uniformly distributed GAGs.[31] Its pore size is in the 500 nm range[31] that imposes negligible steric hindrance on exosome diffusion. Intravitreal injections of exosomes in mice have demonstrated their ability to transport through the VH and reach the retina.[22,23,87] Similarly, 200 nm-sized PEG-functionalized polystyrene nanoparticles exhibited 2× faster diffusivity in VH than their non-PEGylated counterparts.[31] When functionalized with amines to induce cationic surface charge between +7 and +39 mV, a majority of these particles became immobile and were trapped within the VH.[30,31] In healthy VH, the cationic-motif-modified exosomes demonstrated stronger binding interactions with HA resulting in a 3-fold slower average diffusivity (P_A) compared to unmodified exosomes. This was corroborated by microscale thermophoresis data that measured significantly stronger binding affinity of cationic-motif-modified exosomes when compared to that of unmodified exosomes (K_d, Exo-Av: 0.34 μM, Exo-CPC: 0.73 μM *vs.* Exo: 1.48 μM). It is important to note that despite their slowed transport, the cationic-motif-modified exosomes can transport across the VH compartment as their binding to HA is weak and reversible in nature. They also do not experience steric hindrance owing to their smaller size than the VH pores. Recent work has shown that extracellular vesicles are capable of deforming and thus can penetrate through the decellularized scaffolds of pore size smaller than their diameter.[88] The slowed transport through the

VH offers an opportunity for applications in forming intravitreal drug depots for sustained delivery of encapsulated drugs while also targeting the retina. Average diffusivities of cationic-motif-modified exosomes, as expected, increased by 6 times in GAG-depleted VH recapitulating advanced vitreous liquefaction observed in an 80-year-old patient, and by 2 times compared to unmodified exosomes owing to the diminished level of charge-based binding and the presence of hydrophilic PEGs that reduced binding within hydrophobic pockets of collagen fibrils (Fig. 6(D)-(i), (ii) and Table 4). As such, exosomes have the potential to rapidly transport through an aged VH to reach the retina for applications in delivery of small molecule and gene-based therapeutics. There are little to no enzymes or immune cells in the VH due to the acellular and avascular nature of the tissue that can cause exosome degradation;[89] however, their stability *in vivo* should be evaluated in future studies.

The final ocular barrier is the retina itself. Exo-CPC showed a 20-fold stronger presence in the GCL and 10-fold higher uptake in the ONL of porcine retinas compared to unmodified exosomes (Fig. 7(A)). This increased penetration depth and uptake can be attributed to the increasing concentration of chondroitin sulfate GAGs from GCL to the ONL (Fig. 1). Exo-CPC also

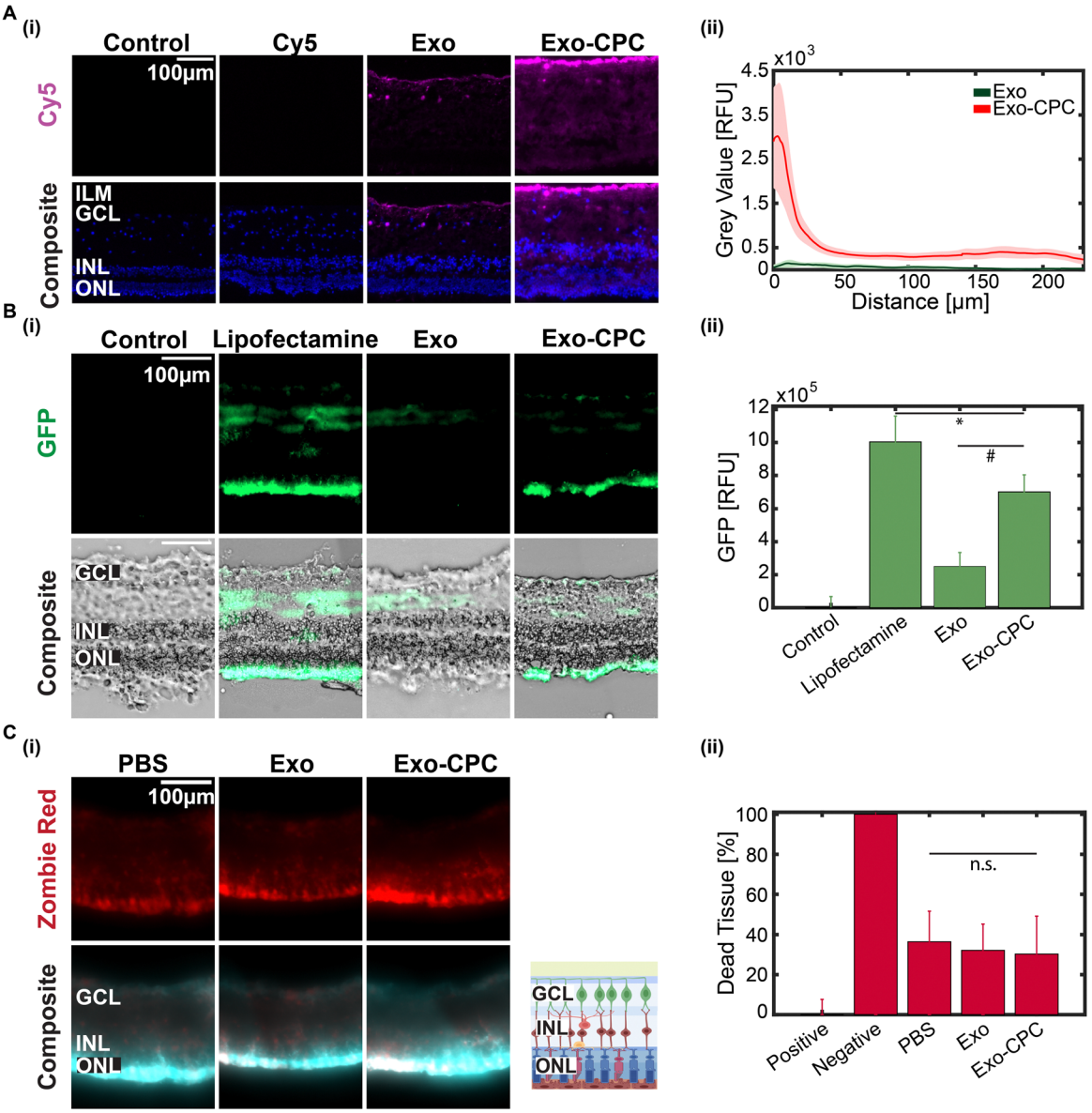

Fig. 7 (A) (i) Representative DAPI and Cy5 images of retinal explants incubated for 24 hours with PBS, Cy5, unmodified Exo, and Exo-CPC. (ii) Average transport rate profiles of unmodified Exo (green) and Exo-CPC (red) across retinal explants cells (B) (i) Representative images of retinal explants transfected with eGFP mRNA loaded lipofectamine, Exo, and Exo-CPC. (ii) Total GFP fluorescence across explants. *$p < 0.05$ compared to lipofectamine. #$p < 0.05$ compared to unmodified Exo. (C) (i) Representative images of live/dead assay on retinal explants stained with Zombie Red and Calbryte AM. A Diagram of key retinal layers included for reference. (ii) Percent of dead tissue after 24-hour incubation. Abbreviations: Inner limiting membrane (ILM), Ganglion cell layer (GCL), Inner neuronal layer (INL), Outer neuronal layer (ONL).

resulted in 3× higher transfection efficiency compared to unmodified exosomes likely due to the increased contact time with the anionic cell layer which induced endocytosis and micropinocytosis pathways.[74–77,79] Moreover, the higher GAG content in the ONL potentially contributed to the preferential transfection of photoreceptors by Exo-CPC (Fig. 7(B)-(i)). Only Exo-CPC was evaluated here as Exo-Av formulation suffered from ionic crosslinking-induced aggregation.

Porcine retinas were used in this study because of their similarity in organization and thickness to that of humans. Introducing a high density of cationic charges comes at the risk of charge shielding within the negatively charged cornea and lens that can cause deswelling,[34,49,90] which may ultimately result in blurry vision.[61,91] Extensive published work has established milk-exosomes as safe, non-immunogenic and stable carriers, and our group has demonstrated the safety of CPCs in high doses in negatively charged tissues like cartilage.[37,43,74] Similarly, in our current work, the size and morphology of exosomes is not significantly affected post modification (Fig. 3 and Table 1). Furthermore, cationic-motif-modified exosomes do not induce significant corneal or lens deswelling. Additionally, Exo-CPC was safe to use as it did not impact retinal explant viability.

A limitation of this study is the use of *ex vivo* corneal explants. The corneal epithelial cell layer is the limiting step for drug transport and the endothelial cell layer is responsible for regulating the water content within the tissue; both die once the tissue is harvested.[67] Additionally, the lack of a viable corneal endothelial cell layer may have had an impact on the swelling pressure measurements that could not be accounted for. Also, it is important that the rate of transport of exosomes across cornea is faster than its clearance rate following topical administration. Thus, the impact of dynamic barriers, like tear film and aqueous humor, on transport and transfection efficacy of cationic-motif-modified exosomes should be evaluated *in vivo* in future studies. Moreover, the tolerance of each ocular tissue to higher doses exosomes doses should be assessed.

5 Conclusions

In summary, these findings, for the first time, demonstrate the potential of milk-derived cationic-motif-modified exosomes for mRNA delivery to photoreceptors in the retina *via* the topical route. Exo-CPC has the potential for targeting several ocular tissues *via* the topical route by taking advantage of GAG and water content for delivery of anti-inflammatory small molecule drugs and gene-based therapeutics and can be applied in the treatment of diabetic retinopathy, age-related macular degeneration, or glaucoma.

Author contributions

Héctor Millán Cotto designed and executed all the experiments and wrote the manuscript. Tanvi Pathrikar and Helna Mary supported milk exosome harvest, surface modification, and mRNA loading. Bill Hakim supported one-dimensional corneal transport, mechanical testing, and microscale thermophoresis measurements. Hengli Zhang supported fluorescent recovery after photobleaching measurements and performed flow cytometry measurements and transmission electron microscopy imaging. Rebecca Carrier, Peng Zhao, and Ronak Ansaripour supported retinal explant model design, harvesting, and cryosectioning. Rouzbeh Amini supported cornea, lens, and vitreous humor harvesting. Ambika Bajpayee conceived the idea, procured funding, designed experiments, oversaw data analysis and writing of the manuscript. All authors were involved in writing, reviewing, and approving the final version of the manuscript.

Data availability

The data supporting this article have been included as part of the ESI.†

Conflicts of interest

There are no conflicts to declare.

Acknowledgements

We thank the Institute for Chemical Imaging of Living Systems at Northeastern University for consultation and imaging support. This study was supported by the National Science Foundation (NSF) CAREER Award 2141841 and by the National Institute of Health (NIH) Trailblazer R21 grant EB028385.

References

1 GBD 2019 Blindness and Vision Impairment Collaborators, *Lancet Glob. Health*, 2021, **9**, e144–e160.
2 M. Tawfik, F. Chen, J. L. Goldberg and B. A. Sabel, *Naunyn-Schmiedebergs Arch. Pharmakol.*, 2022, **395**, 1477–1507.
3 G. A. Peyman, E. M. Lad and D. M. Moshfeghi, *Retina*, 2009, **29**, 875–912.
4 R. Amini, V. H. Barocas, H. P. Kavehpour and J. P. Hubschman, *Retina*, 2011, **31**, 1656–1663.
5 L. Gsellman and R. Amini, *Invest. Ophthalmol. Vis. Sci.*, 2016, **57**, 3340.
6 N. Rashidi, V. S. Thomas and R. Amini, *Transl. Vis. Sci. Technol.*, 2019, **8**, 4.
7 D. Khiev, Z. A. Mohamed, R. Vichare, R. Paulson, S. Bhatia, S. Mohapatra, G. P. Lobo, M. Valapala, N. Kerur, C. L. Passaglia, S. S. Mohapatra and M. R. Biswal, *Nanomaterials*, 2021, **11**, 173.
8 D. A. Lee and E. J. Higginbotham, *Am. J. Health-Syst. Pharm.*, 2005, **62**, 691–699.
9 J. Lusthaus and I. Goldberg, *Med. J. Aust.*, 2019, **210**, 180–187.
10 W. Zhang, M. R. Prausnitz and A. Edwards, *J. Controlled Release*, 2004, **99**, 241–258.

11 F. T. Fraunfelder and S. M. Meyer, *J. Ocul. Pharmacol. Ther.*, 1987, **3**, 177–184.
12 M. Löscher, C. Seiz, J. Hurst and S. Schnichels, *Pharmaceutics*, 2022, **14**, 134.
13 D. M. Pegtel and S. J. Gould, *Annu. Rev. Biochem.*, 2019, **88**, 487–514.
14 S. Samanta, S. Rajasingh, N. Drosos, Z. Zhou, B. Dawn and J. Rajasingh, *Acta Pharmacol. Sin.*, 2018, **39**, 501–513.
15 S. E. L. Andaloussi, S. Lakhal, I. Mäger and M. J. A. Wood, *Adv. Drug Delivery Rev.*, 2013, **65**, 391–397.
16 D. Pollalis, D. Kim, G. K. G. Nair, C. Kang, A. V. Nanda and S. Y. Lee, *Cells*, 2022, **11**, 2573.
17 M. R. Warren, C. Zhang, A. Vedadghavami, K. Bokvist, P. K. Dhal and A. G. Bajpayee, *Biomater. Sci.*, 2021, **9**, 4260–4277.
18 D. Pan, X. Chang, M. Xu, M. Zhang, S. Zhang, Y. Wang, X. Luo, J. Xu, X. Yang and X. Sun, *J. Chem. Neuroanat.*, 2019, **96**, 134–139.
19 R. Kar, R. Dhar, S. Mukherjee, S. Nag, S. Gorai, N. Mukerjee, D. Mukherjee, R. Vatsa, M. Chandrakanth Jadhav, A. Ghosh, A. Devi, A. Krishnan and N. D. Thorat, *ACS Biomater. Sci. Eng.*, 2023, **9**, 577–594.
20 K. D. Popowski, B. López de Juan Abad, A. George, D. Silkstone, E. Belcher, J. Chung, A. Ghodsi, H. Lutz, J. Davenport, M. Flanagan, J. Piedrahita, P.-U. C. Dinh and K. Cheng, *J. Extracell. Vesicles*, 2022, **1**, 100002.
21 S. J. Wassmer, L. S. Carvalho, B. György, L. H. Vandenberghe and C. A. Maguire, *Sci. Rep.*, 2017, **7**, 45329.
22 A. R. Hajrasouliha, G. Jiang, Q. Lu, H. Lu, H. J. Kaplan, H.-G. Zhang and H. Shao, *J. Biol. Chem.*, 2013, **288**, 28058–28067.
23 B. Mead and S. Tomarev, *Stem Cells Transl. Med.*, 2017, **6**, 1273–1285.
24 S. L. Law, K. J. Huang and C. H. Chiang, *J. Controlled Release*, 2000, **63**, 135–140.
25 S. Kakkar, M. Singh, S. Mohan Karuppayil, J. S. Raut, F. Giansanti, L. Papucci, N. Schiavone, T. C. Nag, N. Gao, F.-S. X. Yu, M. Ramzan and I. P. Kaur, *J. Drug Targeting*, 2021, **29**, 631–650.
26 B. P. Danysh and M. K. Duncan, *Exp. Eye Res.*, 2009, **88**, 151–164.
27 J. F. Hejtmancik and A. Shiels, *Prog. Mol. Biol. Transl. Sci.*, 2015, **134**, 119–127.
28 J. R. Sabah, H. Davidson, E. N. McConkey and L. Takemoto, *Mol. Vision*, 2004, **10**, 254–259.
29 J. S. Friedenwald, *Arch. Ophthalmol.*, 1930, **3**, 182.
30 B. T. Käsdorf, F. Arends and O. Lieleg, *Biophys. J.*, 2015, **109**, 2171–2181.
31 Q. Xu, N. J. Boylan, J. S. Suk, Y.-Y. Wang, E. A. Nance, J.-C. Yang, P. J. McDonnell, R. A. Cone, E. J. Duh and J. Hanes, *J. Controlled Release*, 2013, **167**, 76–84.
32 M. M. Le Goff and P. N. Bishop, *Eye*, 2008, **22**, 1214–1222.
33 E. Pacella, F. Pacella, G. De Paolis, F. R. Parisella, P. Turchetti, G. Anello and C. Cavallotti, *Ophthalmol. Eye Dis.*, 2015, **7**, OED.S17204.
34 S. R. Eisenberg and A. J. Grodzinsky, *J. Orthop. Res.*, 1985, **3**, 148–159.
35 P. N. Bishop, *Encyclopedia of the Eye*, Elsevier, 2010, pp. 37–43.
36 C. Zhang, H. Zhang, H. A. Millán Cotto, T. L. Boyer, M. R. Warren, C.-M. Wang, J. Luchan, P. K. Dhal, R. L. Carrier and A. G. Bajpayee, *Biomater. Sci.*, 2024, **12**, 634–649.
37 C. Zhang, T. V. Pathrikar, H. M. Baby, J. Li, H. Zhang, A. Selvadoss, A. Ovchinnikova, A. Ionescu, S. Chubinskaya, R. E. Miller and A. G. Bajpayee, *Small Methods*, 2024, e2301443.
38 C. Zhang, T. He, A. Vedadghavami and A. G. Bajpayee, *MethodsX*, 2020, **7**, 100882.
39 T. He, C. Zhang, T. Colombani, S. A. Bencherif, R. M. Porter and A. G. Bajpayee, *Osteoarthr. Cartilage*, 2023, **31**, 187–198.
40 J. Li, S. Shi, X. Zhang, S. Ni, Y. Wang, C. A. Curcio and W. Chen, *Invest. Ophthalmol. Vis. Sci.*, 2012, **53**, 5675.
41 S. di Lauro, D. Rodriguez-Crespo, M. J. Gayoso, M. T. Garcia-Gutierrez, J. C. Pastor, G. K. Srivastava and I. Fernandez-Bueno, *Mol Vis*, 2016, **22**, 243.
42 V. Alarautalahti, S. Ragauskas, J. J. Hakkarainen, H. Uusitalo-Järvinen, H. Uusitalo, J. Hyttinen, G. Kalesnykas and S. Nymark, *Invest. Ophthalmol. Visual Sci.*, 2019, **60**, 1914–1927.
43 A. Vedadghavami, E. K. Wagner, S. Mehta, T. He, C. Zhang and A. G. Bajpayee, *Acta Biomater.*, 2019, **93**, 258–269.
44 A. G. Bajpayee, C. R. Wong, M. G. Bawendi, E. H. Frank and A. J. Grodzinsky, *Biomaterials*, 2014, **35**, 538–549.
45 A. Vedadghavami, S. Mehta and A. G. Bajpayee, *J. Visualized Exp.*, 2020, DOI: **10.3791/61340-v**.
46 A. G. Bajpayee and A. J. Grodzinsky, *Nat. Rev. Rheumatol.*, 2017, **13**, 183–193.
47 A. Vedadghavami, C. Zhang and A. G. Bajpayee, *Nano Today*, 2020, **34**, 100898.
48 M. R. Warren, A. Vedadghavami, S. Bhagavatula and A. G. Bajpayee, *Biophys. J.*, 2022, **121**, 3542–3561.
49 S. R. Eisenberg and A. J. Grodzinsky, *J. Biomech. Eng.*, 1987, **109**, 79–89.
50 S. Krag, T. Olsen and T. T. Andreasse, *Invest. Ophthalmol. Visual Sci.*, 1997, **38**, 357–563.
51 M. R. Warren and A. G. Bajpayee, *Bioelectricity*, 2022, **4**, 248–258.
52 E. Han, S. S. Chen, S. M. Klisch and R. L. Sah, *Biophys. J.*, 2011, **101**, 916–924.
53 X. Lux Lu, C. Miller, F. H. Chen, X. Edward Guo and V. C. Mow, *J. Biomech.*, 2007, **40**, 2434–2441.
54 S. Mehta, T. L. Boyer, S. Akhtar, T. He, C. Zhang, A. Vedadghavami and A. G. Bajpayee, *Osteoarthr. Cartilage*, 2023, **31**, 780–792.
55 A. Vedadghavami, T. He, C. Zhang, S. M. Amiji, B. Hakim and A. G. Bajpayee, *Acta Biomater.*, 2022, **151**, 278–289.
56 C. D. DiDomenico, M. Lintz and L. J. Bonassar, *Nat. Rev. Rheumatol.*, 2018, **14**, 393–403.
57 R. Gaudana, H. K. Ananthula, A. Parenky and A. K. Mitra, *AAPS J.*, 2010, **12**, 348–360.
58 K. M. Hämäläinen, K. Kananen, S. Auriola, K. Kontturi and A. Urtti, *Invest. Ophthalmol. Visual Sci.*, 1997, **38**, 627–634.
59 E. M. Espana and D. E. Birk, *Exp. Eye Res.*, 2020, **198**, 108137.

60 M. Sridhar, *Indian J. Ophthalmol.*, 2018, **66**, 190.
61 X. Ruan, Z. Liu, L. Luo and Y. Liu, *BMJ Open Ophthalmol.*, 2020, **5**, e000459.
62 Y. Komai and T. Ushiki, *Invest. Ophthalmol. Vis. Sci.*, 1991, **32**, 2244–2258.
63 G. S. Manning, *J. Chem. Phys.*, 1969, **51**, 924–933.
64 G. S. Manning, *J. Phys. Chem. B*, 2007, **111**, 8554–8559.
65 C. H. Dohlman, B. O. Hedbys and S. Mishima, *Invest. Ophthalmol. Visual Sci.*, 1962, **1**, 158–162.
66 B. O. Hedbys and C. H. Dohlman, *Exp. Eye Res.*, 1963, **2**, 122–129.
67 A. O. Eghrari, S. A. Riazuddin and J. D. Gottsch, in *Progress in Molecular Biology and Translational Science*, eds. J. F. Hejtmancik and J. M. Nickerson, Academic Press, 2015, pp.7–23.
68 S. J. Tuft and D. J. Coster, *Eye*, 1990, **4**, 389–424.
69 L. Peeters, N. N. Sanders, K. Braeckmans, K. Boussery, J. Van de Voorde, S. C. De Smedt and J. Demeester, *Invest. Ophthalmol. Vis. Sci.*, 2005, **46**, 3553.
70 K. Braeckmans, L. Peeters, N. N. Sanders, S. C. De Smedt and J. Demeester, *Biophys. J.*, 2003, **85**, 2240–2252.
71 R. Y. Foos and N. C. Wheeler, *Ophthalmology*, 1982, **89**, 1502–1512.
72 J. Sebag, *Encyclopedia of the Eye*, Elsevier Science and Technology, St. Louis, MO, 1st edn, 2010, pp.307–315.
73 M. Inatani and H. Tanihara, *Prog. Retinal Eye Res.*, 2002, **21**, 429–447.
74 A. Vedadghavami, B. Hakim, T. He and A. G. Bajpayee, *Arthritis Res. Ther.*, 2022, **24**, 172.
75 C. C. Young, A. Vedadghavami and A. G. Bajpayee, *Bioelectricity*, 2020, **2**, 68–81.
76 J. F. Liang and V. C. Yang, *Biochem. Biophys. Res. Commun.*, 2005, **335**, 734–738.
77 C. Foged and H. M. Nielsen, *Expert Opin. Drug Delivery*, 2008, **5**, 105–117.
78 C. Foerg, U. Ziegler, J. Fernandez-Carneado, E. Giralt and H. P. Merkle, *Pharm. Res.*, 2007, **24**, 628–642.
79 I. Nakase, A. Tadokoro, N. Kawabata, T. Takeuchi, H. Katoh, K. Hiramoto, M. Negishi, M. Nomizu, Y. Sugiura and S. Futaki, *Biochemistry*, 2007, **46**, 492–501.
80 X. Luan, K. Sansanaphongpricha, I. Myers, H. Chen, H. Yuan and D. Sun, *Acta Pharmacol. Sin.*, 2017, **38**, 754–763.
81 H. Kalra, C. G. Adda, M. Liem, C.-S. Ang, A. Mechler, R. J. Simpson, M. D. Hulett and S. Mathivanan, *Proteomics*, 2013, **13**, 3354–3364.
82 X.-C. Jiang and J.-Q. Gao, *Int. J. Pharm.*, 2017, **521**, 167–175.
83 T. He, C. Zhang, A. Vedadghavami, S. Mehta, H. A. Clark, R. M. Porter and A. G. Bajpayee, *J. Controlled Release*, 2020, **318**, 109–123.
84 T. He, I. Shaw, A. Vedadghavami and A. G. Bajpayee, *Cartilage*, 2022, **13**, 194760352210930.
85 E. K. Wagner, A. Vedadghavami, T. D. Jacobsen, S. A. Goel, N. O. Chahine and A. G. Bajpayee, *Sci. Rep.*, 2020, **10**, 12017.
86 C. Zhang, A. Vedadghavami, T. He, J. F. Charles and A. G. Bajpayee, *ACS Nano*, 2023, **17**, 6649–6663.
87 M. Ma, B. Li, M. Zhang, L. Zhou, F. Yang, F. Ma, H. Shao, Q. Li, X. Li and X. Zhang, *Exp. Eye Res.*, 2020, **191**, 107899.
88 S. Lenzini, R. Bargi, G. Chung and J.-W. Shin, *Nat. Nanotechnol.*, 2020, **15**, 217–223.
89 H. Lund-Andersen, J. Sebag, B. Sander and M. La Cour, *Adv. Organ Biol.*, 2005, 181–194.
90 E. Martinez-Enriquez, A. de Castro, A. Mohamed, N. G. Sravani, M. Ruggeri, F. Manns and S. Marcos, *Invest. Ophthalmol. Vis. Sci.*, 2020, **61**, 11.
91 Y. S. Rabinowitz, *Surv. Ophthalmol.*, 1998, **42**, 297–319.

